technical transactions

No. 2025/031

mechanics

Paradigm

Identification of Motion Model Parameters for a Small Hybrid--Propelled Unmanned Underwater Vehicle (HUUV)

Tomasz Talarczyk
tomasz.talarczyk@pk.edu.pl | https://orcid.org/0000-0002-6010-4333
Marcin Morawski
marcin.morawski@pk.edu.pl | https://orcid.org/0000-0002-7078-2795
Marcin Malec
marcin.malec@pk.edu.pl | https://orcid.org/0000-0001-5232-7425
Michał Garncarz
michal.garncarz@pk.edu.pl | https://orcid.org/0009-0001-5663-8703
Cracow University of Technology, Faculty of Mechanical Engineering,
Chair of Production Engineering

Scientific Editor: Grzegorz Filo,
Cracow University of Technology
Technical Editor: Aleksandra Urzędowska,
Cracow University of Technology Press
Typesetting: Anna Pawlik,
Cracow University of Technology Press

Received: November 5, 2025
Accepted: December 17, 2025

Data Availability Statement: All relevant data are within the paper and its Supporting Information files.

Competing interests: The authors have declared that no competing interests exist.

Citation: Talarczyk, T., Morawski, M., Malec, M., Garncarz, M. (2025). Identification of Motion Model Parameters for a Small Hybrid-Propelled Unmanned Underwater Vehicle (HUUV), *e2025031*. https://doi.org/10.37705/TechTrans/e2025031

Abstract

This paper presents the development of a motion model for a hybrid-propelled unmanned underwater vehicle (HUUV) and its verification through MATLAB® simulations and experimental tests conducted with a real vehicle in a swimming pool. The motion tracking method, utilizing a GoPro Hero 6 camera and Tracker® software, was employed to measure the vehicle's forward velocities, sideslip angles, and circulation radii under various thrust settings. The experimental results were compared with those obtained from simulations using the same thruster configurations. The proposed model is intended to support the development of control algorithms for groups of HUUVs.

Keywords: HUUV model parameters identification, underwater vehicle motion analysis

1. Introduction

Mathematical modelling of a newly designed and build underwater vehicle is an essential first step in the subsequent development of its control system. Understanding the vehicle's dynamics helps to implement its model in simulations for developing control laws and tuning parameters prior to experimental research. This approach becomes even more important when developing algorithms for the coordinated movement of multiple underwater vehicles intended to perform a common task.

One of the methods of modelling aquatic vehicles was originally developed by Thor Inge Fossen in (Fossen, 1994), and later refined in (Fossen, 2011). It has been widely used in the field of marine engineering (Piskur et al., 2025). This six--degree-of-freedom (6 DOF) model follows the SNAME notation (Society of Naval Architects and Marine Engineers, 1950) and describes rigid body motion through water taking into account hydrodynamic drag and added masses represented as various coefficients in the equations of motion. Their precise identification often poses a challenge; thus, some simplifications are unavoidable. The most common assumptions include a torpedo-like hull shape with three main planes of symmetry, a small metacentric height, and planar motion (Tran et al., 2016; Tae Kyu Ha et al., 2008; Da Silva et al., 2007). These simplifications reduce the hydrodynamic coupling effects between different motion axes in the local coordinate system. Trusters and control surfaces are modelled as a forces and moments applied at specific places of the hull, while model coefficients are calculated analytically (Shrivastava, Karthikeyan and Rajagopal, 2021). CFD analysis of transient flow conditions for determining vehicle model parameters are also increasingly popular (Suzuki et al., 2013; Moelyadi and Riswandi, 2018; Piotr Szymak et al., 2021; Foroushani and Sabzpooshani, 2021). Parameters obtained either analytically or numerically must be verified experimentally on a real vehicle or it's simplified scaled model (Sakaki and Sadeghian Kerdabadi, 2020a). One such experimental method uses PMM (Planar Motion Mechanism) tests (Suzuki et al., 2013), in which the vehicle submerged in still water within a towing tank is set into oscillatory motion using an external mechanism, while forces and moments acting on the vehicle are measured simultaneously. Circulating water channels may also be used in those tests, where the vehicle remains stationary and water flow is forced around its hull. PMM tests are particularly effective for determining acceleration-based hydrodynamic coefficients (added mass), as they involve unsteady motion. The increasing development and decreasing costs of advanced CFD software now makes it possible to simulate some aspects of PMM tests numerically (Foroushani and Sabzpooshani, 2021), eliminating the need for costly and sophisticated laboratory equipment.

The aforementioned methods are also very useful in the development and modelling of biomimetic underwater vehicles, which often have asymmetrical rigid hull and elastic fish-like propulsors (Morawski et al., 2018). The lack of three planes of symmetry of the hull and its complex fishlike shape make it difficult to determine hydrodynamic coefficients (Chan and Kang, 2011). Determining the forces and moments generated by oscillating or undulating biomimetic thrusters acting on the rigid hull is, in this case, the most challenging task. Elastic fins and tails are usually considered separately (Jurczyk, Piskur and Szymak, 2020;Piskur et al., 2021) and their influences on vehicle motion is incorporated into the equations as concentrated forces and moments applied at specific points on the hull (Wang et al., 2025a; Przybylski, 2019).

In modelling small unmanned underwater vehicles, either classical or biomimetic, visual tracking methods, image analysis and motion capture techniques pay an important role in measuring the vehicle's motion parameters. They are relatively easy to implement using various camcorders suspended above a swimming pool or submerged in water, along with appropriate software.

https://doi.org/10.37705/TechTrans/e2025031

Typically, short straight-line motions and circular trajectories are measured (Wang et al., 2025b;Xie and Du, 2019) and compared with simulated results.

2. Methods

The HUUV presented in Fig. 1, developed at the Cracow University of Technology, is a low-cost research platform designed for testing and analysing swarm algorithms. Four such vehicles have been constructed to enable group experiments. The vehicle has a cylindrical hull with two screw propellers at the stern and two lateral fins with elastic ends at the bow. Heading control is achieved by differential thrust, whereas the lateral fins can operate in two modes: as elevators or as auxiliary oscillating biomimetic thrusters. Therefore, the term *hybrid* refers to the presence of these two types of propulsion in the HUUV. The mass of the HUUV in air is 19 kg. The vehicle is also equipped with large cylindrical mast in the middle top of the hull and a heavy ballast underneath to provide sufficient static stability. Each vehicle's mast provides information about the positions of other units in the group through light signals generated by RGB LED strips and an onboard camera-based environment analysis system. Additionally, the mast supports basic inter-vehicle communication by transmitting Morse code through LED blinking. For environmental perception, the vehicle employs an ArduCam IMX219 camcorder module equipped with an 8-megapixel 1/4-inch sensor and a wide-angle lens offering a field of view of approximately 155° horizontally and 115° vertically. Although the camera natively supports an image resolution of 3280 × 2464 pixels, the resolution was downscaled in software to 800 × 600 pixels in order to decrease computational load during visual localization. The frame rate was likewise limited to 10 fps. Under these settings, the system is capable of detecting the masts of other vehicles at distances of up to approximately 5 meters. The ArduCam is mounted on a servomotor on top of the mast under transparent dome, enabling its rotation around masts longitudinal axis. This is useful for active seeking of interesting targets, such as other vehicles in a group.

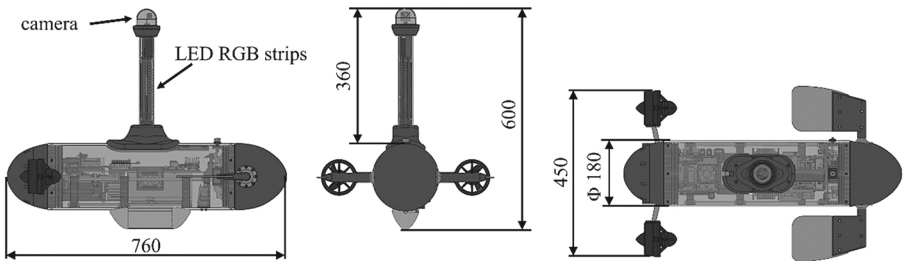

Fig. 1. Views and dimensions of the HUUV (own elaboration)

To obtain the HUUV's motion parameters, experimental studies were conducted in a swimming pool, during which swimming speeds, circulation radii, and the sideslip angle were measured. Motion parameters were recorded using a GoPro Hero 6 camcorder positioned 4 meters above the pool, followed by image analysis in Tracker® software. Two selected point on the hull were tracked to determine the vehicle's orientation. The GoPro camcorder was set to linear mode to reduce the impact of lens distortion. Videos were recorded at 25 fps with a resolution of 1920 × 1080 pixels. The measurement setup showing the GoPro camcorder's position on a simple pendulum is presented in Fig. 2, and the analysis of the recordings in Tracker® software is shown in Fig. 3. The use of a simple pendulum in the camera mounting system above the pool ensures that the footage is captured perpendicularly to the water surface.

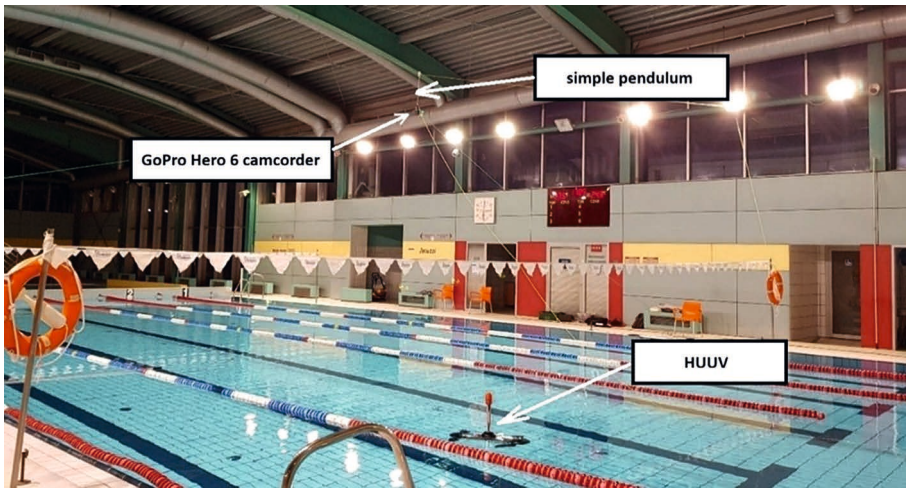

Fig. 2. Visual tracking setup (own elaboration)

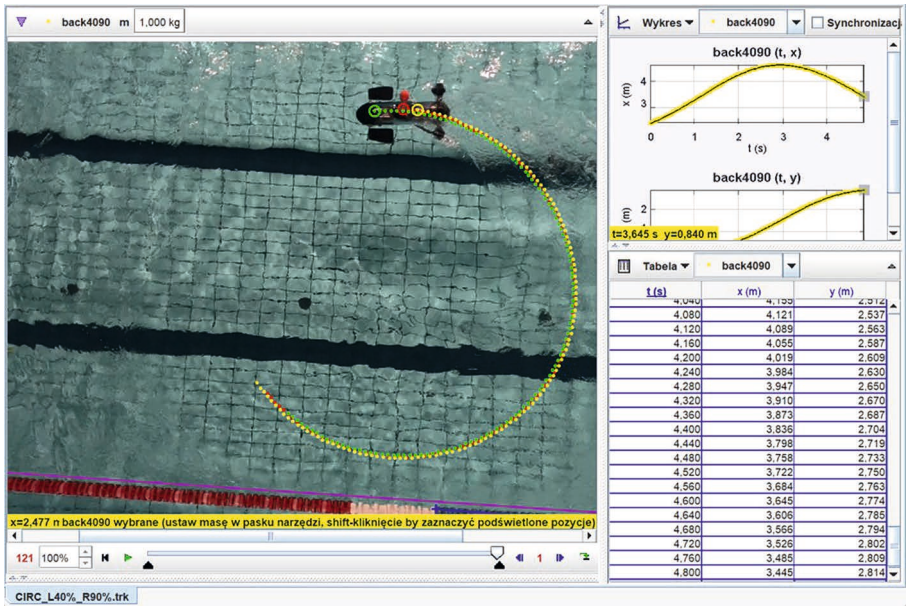

Fig. 3. Vehicle's planar motion analysis (own elaboration)

3. Motion model of HUUV

The limited localization range of the HUUV's visual tracking system necessitates that the vehicles exhibit high manoeuvrability and rapid response capabilities to maintain formation and prevent collisions during deceleration. Consequently, the HUUV's motion cannot be represented solely by a kinematic model. To ensure an accurate description of its behaviour, a dynamic model of motion was formulated for the HUUV based on the general framework proposed by Fossen (Fossen, 1994). It is assumed that the vehicle operate within a common global Cartesian coordinate frame (x_n, y_n, z_n), defined according to North--East-Down (NED) convention. Second, body-fixed cartesian coordinate system (x_b, y_b, z_b) is located at the vehicle's centre of buoyancy as shown in Fig. 4. The x_b axis lies along the main hull and points forward, the z_b axis is perpendicular to it and directed downward, while the y_b axis is orthogonal to both and points toward the port side.

As shown in Fig. 4, the HUUV differs from conventional AUV designs, as it does not exhibit full three-plane symmetry. This is primarily due to the presence of a large mast mounted on the upper central part of the hull. The vehicle remains symmetric with respect to the $(x_b - z_b)$ plane, while the mast introduces asymmetry relative to the $(x_b - y_b)$ plane. To ensure roll and pitch

https://doi.org/10.37705/TechTrans/e2025031

stability, the vehicle's metacentric height was increased by placing heavy ballast at the bottom of the hull. The combination of the asymmetric hull geometry, the elevated metacentric height, and the use of two stern-mounted propellers that operate both as main thrusters and as steering devices results in HUUV motion characterized by nonzero angles of attack and sideslip.

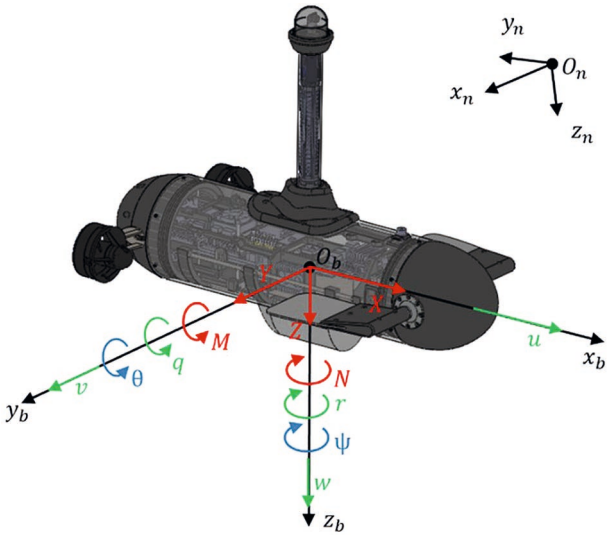

Fig. 4. HUUV with depicted global and body-fixed coordinate frames, main forces and moments acting on the vehicle (red), velocities (green) and angles of orientation (blue) (own elaboration)

A dynamic motion model describing only the submerging behaviour within the $(x_b - z_b)$ plane was previously developed and validated through pool experiments using the real vehicle, as reported in (Talarczyk, 2023a). The same modelling approach was later extended to represent HUUV dynamics in three-dimensional space. The complete set of motion equations is presented in Equation (1). Since the vehicle's substantial metacentric height effectively suppresses roll even during rapid manoeuvres, the roll-related components were neglected, simplifying the full model to five degrees of freedom.

$$\mathbf{M}\cdot\dot{\nu}+\mathbf{C}(\nu)\cdot\nu+\mathbf{D}(\nu)\cdot\nu+\mathbf{g}(\eta)=\tau \tag{1}$$

where parameters of the system are as follows: $\mathbf{M}$ – inertia matrix and added mass matrix $(\mathrm{M}=\mathrm{M}_{RB}+\mathrm{M}_{A})$; $\mathbf{C}(\nu)$ – Coriolis and centripetal matrix $(\mathrm{C}(\nu)=\mathrm{C}_{RB}(\nu)+\mathrm{C}_{A}(\nu))$; $\mathbf{D}(\nu)$ – damping matrix; $\mathbf{g}(\eta)$ – vector of gravitational forces and moments; $\nu=[u\ v\ w\ q\ r]^T$ – vector of linear and angular velocities; $\eta=[x\ y\ z\ \theta\ \psi]^T$ – vector of linear and angular coordinates; $\tau=[X\ Y\ Z\ M\ N]^T$ – vector of forces and moments from thrusters and lateral fins,

$$\mathrm{M}=\begin{bmatrix} m+m_x & 0 & 0 & (m-m_z)z_{CG} & 0 \\ 0 & m+m_y & 0 & 0 & m_{y_r} \\ 0 & 0 & m+m_z & m_{z_q} & 0 \\ (m-m_z)z_{CG} & 0 & J_{y_w} & I_y+J_y & 0 \\ 0 & I_{z_v} & 0 & 0 & I_z+J_z \end{bmatrix},$$

$$\mathrm{D}(\nu)\nu=\begin{bmatrix} F_x \\ F_y \\ F_z \\ M_y \\ M_z \end{bmatrix}, \qquad \mathrm{g}(\eta)=-\begin{bmatrix} -(F_w-F_B)\sin(\theta) \\ 0 \\ (F_w-F_B)\cos(\theta) \\ z_{CG}F_w\sin(\theta) \\ 0 \end{bmatrix}$$

$$C(\nu)=$$

$$=\begin{bmatrix} 0 & 0 & 0 & (m+m_z)w+m_{z_q}q & -(m+m_y)v-m_{y_r}r \\ 0 & 0 & 0 & mz_{CG}r & (m+m_x)u-m_z z_{CG}q \\ 0 & 0 & 0 & -(m-m_z)z_{CG}q-(m+m_x)u & 0 \\ -(m+m_z)w-m_{z_q}q & -mz_{CG}r & (m-m_z)z_{CG}q+(m+m_x)u & 0 & m_z z_{CG}v \\ (m+m_y)v+m_{y_r}r & -(m+m_x)u+m_z z_{CG}q & 0 & -m_z z_{CG}v & 0 \end{bmatrix}$$

where: m_x, m_y, m_z, J_y, J_z – added masses in the x, y, and z directions, around the y and z axes, respectively obtained from the analytical analysis of the hull geometry and data found in the literature (Newman, 1977a); $J_{z_v}, J_{y_w}, m_{z_q}, m_{y_r}$ – added mass coupling terms; F_w, F_B – gravity and buoyancy force respectively; z_{CG} – distance between centre of gravity and centre of buoyancy,

To determine the damping force vector while accounting for vehicle motion with nonzero angles of attack and sideslip, the velocity vector was defined as illustrated in Fig. 5, following the SNAME notation. The angle of attack, denoted as α, is defined as the angle between the x_b axis and the projection of the velocity vector V onto the $(x_b - z_b)$ plane. Similarly, the sideslip angle β is the angle between the x_b axis and the projection of V onto the $(x_b - y_b)$ plane. The signs of both α and β are determined according to the right-hand rule. The vehicle's velocity, attack and sideslip angles can be calculated based on equations (2), (3) and (4).

$$\mathbf{V}=\sqrt{\mathbf{u}^2+\mathbf{v}^2+\mathbf{w}^2} \tag{2}$$

$$\alpha=\arctan\left(\frac{w}{u}\right) \tag{3}$$

$$\beta=\arcsin\left(\frac{v}{V}\right) \tag{4}$$

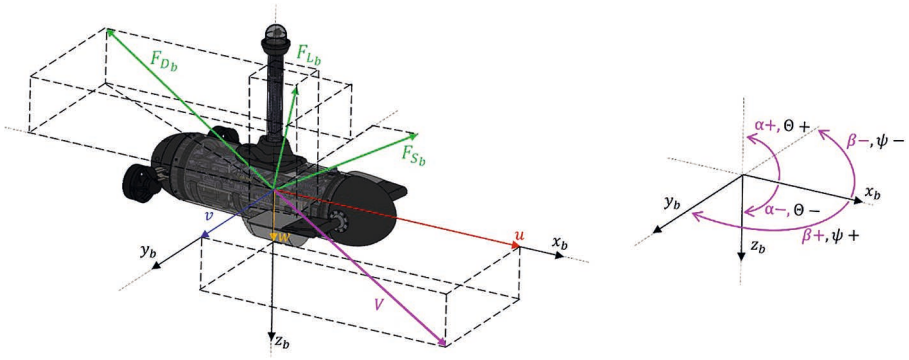

Fig. 5. HUUV velocity vector $\mathbf{V}$ with angle of attack α, angle of sideslip β and hull forces: drag F_{D_b}, lift F_{L_b} and side F_{S_b} (own elaboration)

To calculate the damping forces acting on the HUUV, the computations were divided into two parts: the forces acting on the hull with the control surfaces in a neutral position, and forces generated by the submerged control surfaces when deflected from the neutral position.

Equations (5–12) allows to calculate damping forces and moments acting on the hull with the control surfaces in a neutral position. In equation (6) the F_{L_b} component in y_b axis and in equation (7) F_{S_b} component in z_b axis are negligibly small due to vehicle's high roll stability and were therefore omitted.

$$F_{D_{b_{x_b}}}=\cos(\alpha)\cos(\beta)F_{D_b}-\sin(\beta)F_{S_b}+\sin(\alpha)\cos(\beta)F_{L_b} \tag{5}$$

https://doi.org/10.37705/TechTrans/e2025031

$$F_{D_{b_{y_b}}} = \sin(\beta) F_{D_b} + \cos(\beta) F_{S_b} \tag{6}$$

$$F_{D_{b_{z_b}}} = \sin(\alpha)\cos(\beta) F_{D_b} + \cos(\alpha) F_{L_b} \tag{7}$$

$$\mathbf{F}_{D_b}(\mathrm{V}, \alpha, \beta) = 0.5\rho \mathrm{V}^2 \mathrm{A}_b \mathrm{C}_{D\alpha\beta} \tag{8}$$

$$\mathbf{F}_{S_b}(\mathrm{V}, \beta) = 0.5\rho \mathrm{V}^2 \mathrm{A}_b \mathrm{C}_{S\beta} \tag{9}$$

$$\mathbf{F}_{L_b}(\mathrm{V}, \alpha) = 0.5\rho \mathrm{V}^2 \mathrm{A}_b \mathrm{C}_{L\alpha} \tag{10}$$

$$\mathbf{M}_{q_b}(\mathrm{V}, \alpha, q) = 0.5\rho \mathrm{V}^2 \mathrm{A}_b \mathrm{LC}_{m\alpha} + \mathrm{M}_{mq} \tag{11}$$

$$\mathbf{M}_{r_b}(\mathrm{V}, \beta, r) = 0.5\rho \mathrm{V}^2 \mathrm{A}_b \mathrm{LC}_{m\beta} + \mathrm{M}_{mr} \tag{12}$$

where: A_b – area of the vehicle's cross section projected on the direction of the velocity vector V; L – vehicle's length; $\mathrm{C}_{D\alpha\beta}, \mathrm{C}_{S\beta}, \mathrm{C}_{L\alpha}, \mathrm{C}_{m\alpha}, \mathrm{C}_{m\beta}, \mathrm{M}_{mq}, \mathrm{M}_{mr}$ – dumping coefficients obtained from the CFD analysis of the vehicle.

The forces generated by the submerged control surfaces when deflected from the neutral position by an angle δ are shown in Fig. 6 and can be calculated using equations (13–17).

$$F_{D_{f_{z_b}}} = \sin(\alpha) F_{D_f} + \cos(\alpha) F_{L_f} \tag{13}$$

$$M_{m_{f_{y_b}}} = M_{m_f} + x_f F_{L_f} \tag{14}$$

$$F_{D_f}(\mathrm{V}_{x_b - z_b}, \alpha, \delta) = 0.5\rho \mathrm{V}^2_{x_b - z_b} \mathrm{A}_f \mathrm{C}_{D\delta}(\delta - \alpha) \tag{15}$$

$$F_{L_f}(\mathrm{V}_{x_b - z_b}, \alpha, \delta) = 0.5\rho \mathrm{V}^2_{x_b - z_b} \mathrm{A}_f \mathrm{C}_{L\delta}(\delta - \alpha) \tag{16}$$

$$\mathrm{M}_{m_f}(\mathrm{V}_{x_b - z_b}, \alpha, \delta) = 0.5\rho \mathrm{V}^2_{x_b - z_b} \mathrm{A}_f \mathrm{C}_{M\delta}(\delta - \alpha) \tag{17}$$

where: A_f – reference surface area of the elevator; x_f – distance between elevator's axis of rotation and centre of buoyancy of the vehicle in x_b axis; $\mathrm{C}_{D\delta}, \mathrm{C}_{L\delta}, \mathrm{C}_{M\delta}$ – dumping coefficients obtained from the CFD analysis of the vehicle's elevators.

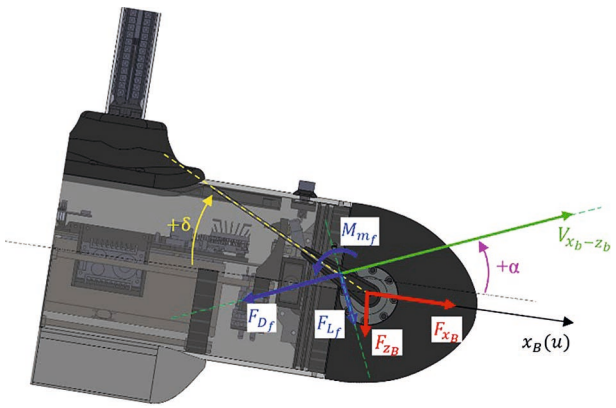

Fig. 6. Forces F_{D_f}, F_{L_f} and moment M_{m_f} acting on the elevator (own elaboration)

Final damping vector $(D(\nu)\nu)$ elements is calculated as a sum of equations (5–12) and (13–17).

$$F_x = F_{D_{b_{x_b}}} \tag{23}$$

$$F_y = F_{D_{b_{y_b}}} \tag{24}$$

$$F_z = F_{D_{b_{z_b}}} + F_{D_{f_{z_b}}} \tag{25}$$

$$M_y = M_{q_b} + M_{m_{f_{y_b}}} \tag{26}$$

$$M_z = M_{r_b} \tag{27}$$

To determine the added mass coefficients in the M_A and $C_A(\nu)$ matrices, analytical calculations were performed following the methodologies presented in (Newman, 1977b), which provides formulas for the added mass of simple geometries, and in (Gracey, 1941), which details the added mass of flat plates. For this purpose, the vehicle geometry was initially simplified into two cylinders representing the hull and the mast, and two flat plates approximating the submerged elevator surfaces, as shown in Fig. 7.

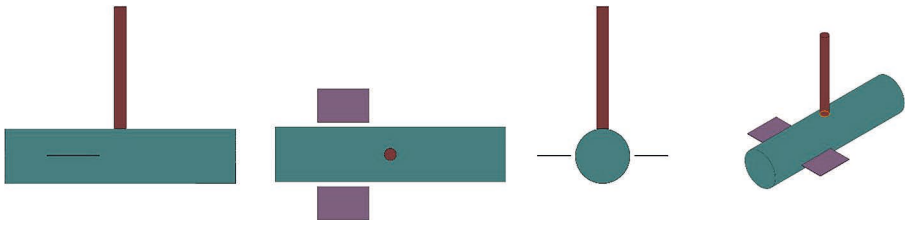

Fig. 7. The vehicle's geometry simplified to cylinders (hull, mast) and flat plates (elevators) for added mass calculation (own elaboration)

Based on this simplification, the added mass components are calculated using equations (28–32). In these equations, the subscripts denote the components as follows: h for the hull, m for the mast, and e for the elevators.

$$m_x = m_{xh} + m_{xm} + m_{xe} = \frac{1}{10}\rho\pi r_h^2 L_h + \rho\pi r_m^2 L_m + 0 \tag{28}$$

$$m_y = m_{yh} + m_{ym} + m_{ye} = \rho\pi r_h^2 L_h + \rho\pi r_m^2 L_m + 0 \tag{29}$$

$$m_z = m_{zh} + m_{zm} + m_{ze} = \rho\pi r_h^2 L_h + 0 + 2k\frac{\pi\rho c^2 b^3}{4} \tag{30}$$

$$J_y = J_{yh} + J_{ym} + J_{ye} = \frac{1}{12}\rho\pi r_h^2 L_h^3 + \frac{1}{3}\rho\pi r_m^2 L_m^3 + 2x_B^2 k'\frac{\pi\rho c^2 b}{4} \tag{31}$$

$$J_z = J_{zh} + J_{zm} + J_{ze} = \frac{1}{12}\rho\pi r_h^2 L_h^3 + 0 + 0 \tag{32}$$

where: r_h, L_h – radius and length of the hull; r_m, L_m – radius and length of the mast; c, b – length and width of the elevators; k – added mass coefficient for a rectangular plate; k' – added moment of inertia coefficient for a rectangular plate.

https://doi.org/10.37705/TechTrans/e2025031

The last four added mass coefficients, $m_{yr}, m_{zq}, J_{yw}, J_{zv}$, are off-diagonal terms and have a smaller influence on the vehicle's overall motion dynamics compared to the diagonal coefficients. Nevertheless, they were included in the vehicle's equations of motion. Their values were estimated based on the dimensional similarity of the HUUV hull to the SNUUV-I (Kim and Choi, 2007) and REMUS (Prestero, 2001) vehicles, for which these coefficients were determined experimentally using planar motion mechanism tests. Based on this approach, the coefficient values were calculated according to equation 33.

$$m_{yr} = m_{zq} = J_{yw} = J_{zv} = \frac{1}{20}\mathrm{m} \tag{33}$$

The vehicle's heading (yaw angle) is controlled by applying differential thrust between the left and right propellers. The thrust force F_{thr} generated by each thruster is determined using equation (34), where c_T represents the control input to the thruster motor, expressed as a percentage of its maximum thrust. The control signal varies from 0 to 100%, with a dead zone between −14% and 14%. The coefficients used in equation (34) were derived from data provided by the thruster manufacturer (Bluerobotics, 2025), obtained under Bollard test conditions, and from experimental results reported in (Lam et al., 2023), where the thrusters were tested in a towing tank at various forward velocities.

$$F_{\text{thr}} = \begin{cases} 0.1654 \cdot c_T - 1.9096 & \text{for } c_T \geq 14 \\ 0 & \text{for } c_T < 14 \text{ and } c_T > -14 \\ 0.1389 \cdot c_T + 1.9096 & \text{for } c_T \leq -14 \end{cases} \tag{34}$$

The control inputs for the thrusters are the total longitudinal thrust c_{T_Σ} and the thrust difference c_{T_Δ}. The control signals for the left and right thrusters are then calculated using equations (35) and (36) as percentages of their maximum thrust values.

$$c_{T_L} = c_{T_\Sigma} - c_{T_\Delta}, \quad c_{T_L} \in \langle -100, 100 \rangle \tag{35}$$

$$c_{T_R} = c_{T_\Sigma} + c_{T_\Delta}, \quad c_{T_R} \in \langle -100, 100 \rangle \tag{36}$$

Based on equations (34), (35) and (36) the force and moment of force acting on the vehicle from its thrusters are calculated using equation (37) and equation (38).

$$X_{\text{thr}} = F_{R_{\text{thr}}}(c_{T_R}) + F_{L_{\text{thr}}}(c_{T_L}) \tag{37}$$

$$N_{\text{thr}} = F_{R_{\text{thr}}}(c_{T_R}) \cdot y_{ct} - F_{L_{\text{thr}}}(c_{T_L}) \cdot y_{ct} \tag{38}$$

where: X_{thr} – force in x_b axis; N_{thr} – moment of force in z_b axis; $F_{R_{\text{thr}}}$, $F_{L_{\text{thr}}}$ – thrust generated by the right and left thruster accordingly; y_{ct} – distance between thruster's axis and x_b axis.

4. Simulation and experimental research

In addition to the analytically derived added masses, the HUUV motion model presented in the previous chapter incorporates hydrodynamic resistance coefficients determined through steady-state CFD simulations performed in SimScale®. The methodology followed the procedures outlined by (Watson,

Webster and Crane, 1993;Sakaki and Sadeghian Kerdabadi, 2020b; Le and Hong, 2021), where the vehicle was positioned at various angles of attack (α) and sideslip (β) relative to the oncoming flow. This approach enabled the estimation of drag, lift, and side forces, as well as moments acting on the vehicle. The considered ranges were ±25° for the angle of attack and 0–25° for the sideslip angle. The computational domain and mesh used for these simulations are shown in Fig. 8. The computational setups for rotational motion about the y_b and z_b axes, modelled using a Moving Reference Frame (MRF), are presented in figures 9 and 10, respectively. Fig. 11 presents the computational domain for vehicle's elevator. Table 1 presents the number of mesh cells in each simulation and characteristic length of the simulated object. All simulations were performed with $k - \omega$ SST turbulent model and Semi-Implicit Method for Pressure-Linked Equations (SIMPLE) algorithm. The simulation results, presented as plots of drag coefficients versus the angles α and β, are shown in figures 12–15 along with interpolation polynomials. Fig. 16 presents pitching and yawing moments about the y_b and z_b axes, respectively, instead of dimensionless coefficients.

Table 1. CFD parameters

Simulation type	Mesh cells (after refinement) [million]	Characteristic length L [m]
Simulation of angles of attack	1,5	0,75
Simulation of sideslip angle	5,3	0,75
Simulation of rotational motion about the y_b	5,5	0,75
Simulation of rotational motion about the z_b	5,1	0,75
Simulation of elevators	4,7	0,2

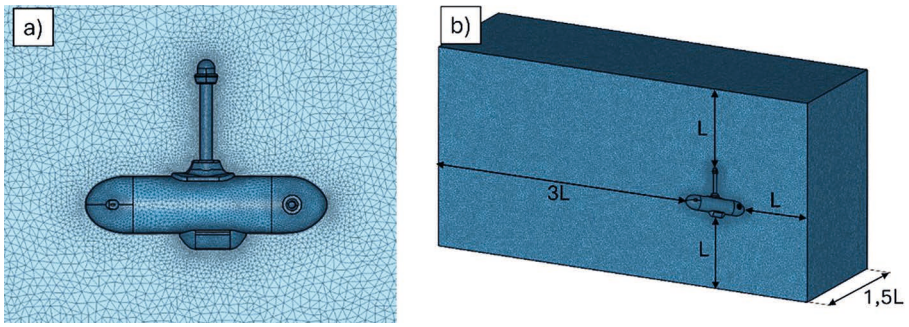

Fig. 8. Simulation of angle of attack (half of domain) and sideslip (full domain). Mesh refinement (a), half of computational domain (b) (own elaboration)

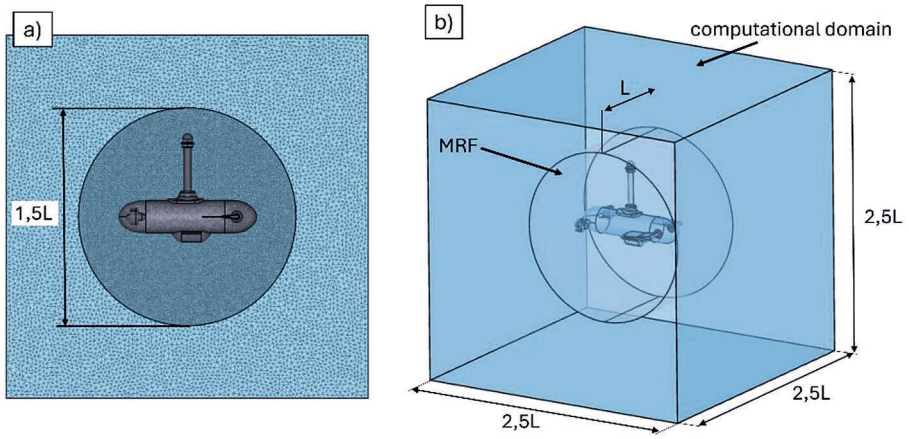

Fig. 9. Simulation of rotational motion around y_b axis. Mesh refinement (a), computational domain with MRF (b) (own elaboration)

https://doi.org/10.37705/TechTrans/e2025031

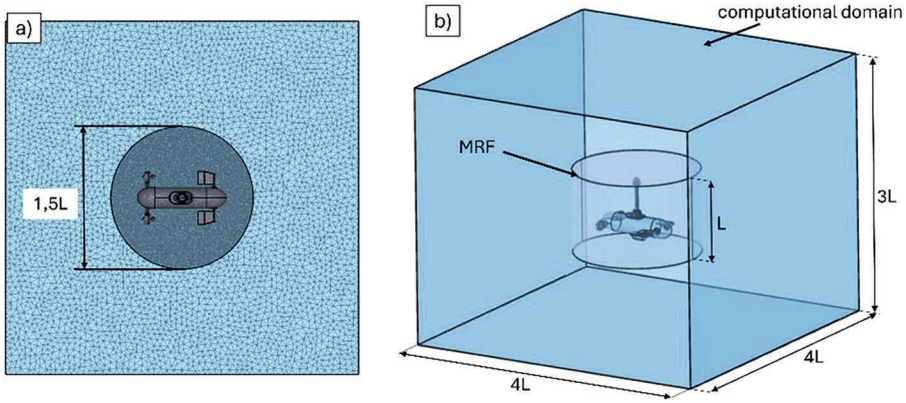

Fig. 10. Simulation of rotational motion around z_b axis. Mesh refinement (a), computational domain with MRF (b) (own elaboration)

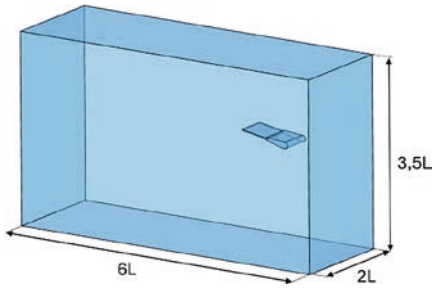

Fig. 11. Computational domain for simulation of forces and moments acting on vehicle's elevator (own elaboration)

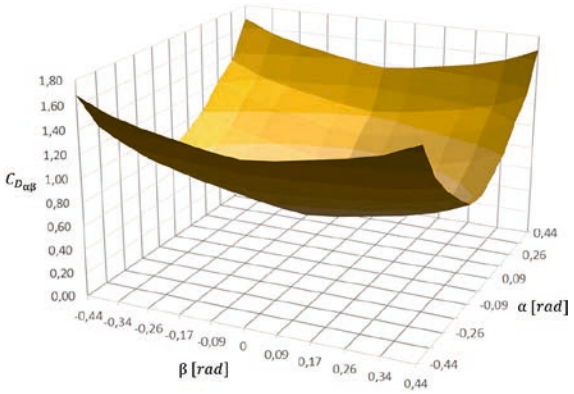

Fig. 12. Drag coefficient $C_{D_{\alpha\beta}}$ versus angles α and β ($C_{D_{\alpha\beta}} \approx C_{D\alpha 0} + C_{D\beta 0}$) (own elaboration)

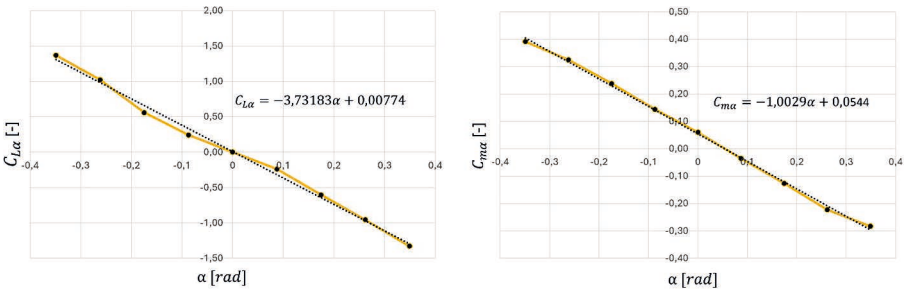

Fig. 13. Lift $C_{L\alpha}$ and moment $C_{m\alpha}$ coefficients versus angle α (own elaboration)

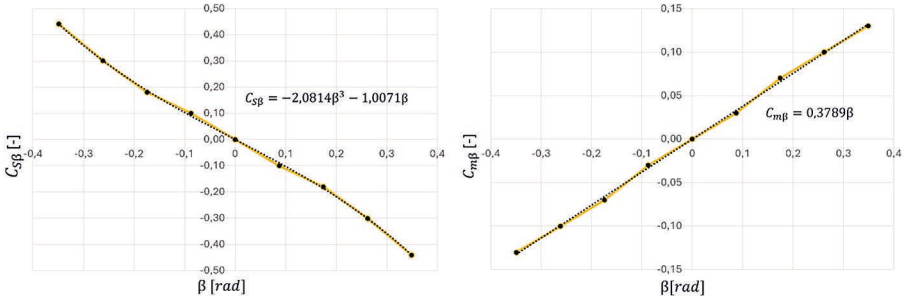

Fig. 14. Side $C_{S\beta}$ and moment $C_{m\beta}$ coefficients versus of angle β (own elaboration)

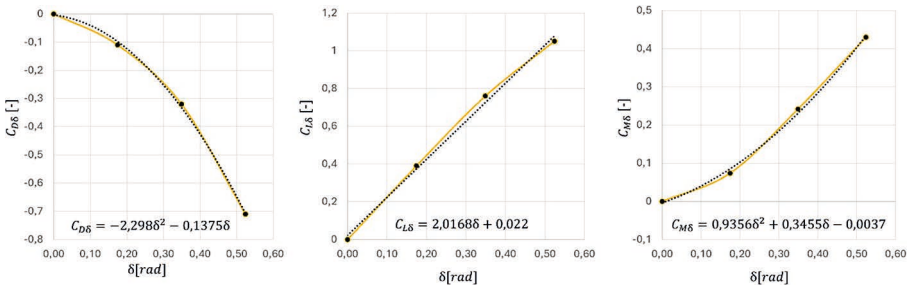

Fig. 15. Drag $C_{D\delta}$, lift $C_{L\delta}$ and moment $C_{M\delta}$ coefficients versus angle δ (own elaboration)

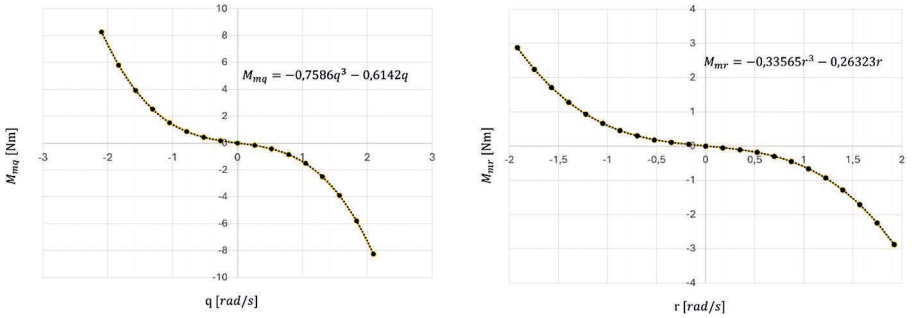

Fig. 16. Pitching moment M_{mq} versus rotational velocity around y_b and yawing moment M_{mr} versus rotational velocity around z_b (own elaboration)

The drag coefficients and moments obtained from the CFD analysis and interpolated using polynomials were applied in the adapted model implemented in the Matlab® simulation of the vehicle moving in $x_n - y_n$ plane. Previous work (Talarczyk, 2023b) describes studies of the vehicle motion in $x_n - z_n$ plane. Various percentages of maximum thrusts of left and right thruster were applied, resulting in either straight or circular motion paths. For circular motion, the right thruster's thrust varied from 20% do 100% with 10 percentage-point increments, while the left thruster's thrust varied from 0% do 40% with 20 percentage-point increment. This allowed the real vehicle in the experiment to follow circular paths with radii ranging from 0.48 m to 1.68 m, which was constrained by the GoPro camcorder's field of view. The sideslip angles β, forward velocities u, and radii of the circular paths were recorder under steady-state conditions of circular motion – twenty eight simulation were performed. Additionally nine simulations of linear forward motion were conducted in which both thrusters operated at equal thrust levels ranging from 20% to 100% in 10-percentage-point increments. The motion patterns of the real HUUV, corresponding to the same thrust settings used in the simulations, were recorded on video and analyzed using Tracker®. Based on the experimental results, the drag coefficients related to the sideslip angle β and the angular velocity r around the z_b axis were tuned using the method of successive approximations. This tuning was achieved by scaling the CFD-derived coefficients $C_{S\beta}$, $C_{m\beta}$ and M_{mr} by a factor of 2. Fig. 17 presents a comparison between the experimentally measured parameters and the simulation results obtained with the tuned drag coefficients, with a color map illustrating the variations in value. Thr relationship between the HUUV's forward velocity and the applied thrust percentage during linear motion is shown in Fig. 18.

https://doi.org/10.37705/TechTrans/e2025031

a) velocity u [m/s] TRACKER

c_{T_R} \ c_{T_L}	0%	20%	30%	40%
20%	0,19			
30%	0,19	0,36		
40%	0,29	0,57		
50%	0,33	0,62	0,79	
60%	0,39	0,65	0,77	1,11
70%	0,45	0,70	0,80	0,99
80%	0,52	0,77	0,88	1,02
90%	0,53	0,78	0,94	1,11
100%	0,61	0,80	0,99	0,93

b) velocity u [m/s] MATLAB

c_{T_R} \ c_{T_L}	0%	20%	30%	40%
20%	0,17			
30%	0,27	0,39		
40%	0,35	0,45		
50%	0,42	0,49	0,62	
60%	0,48	0,54	0,64	0,74
70%	0,53	0,59	0,68	0,77
80%	0,58	0,63	0,71	0,79
90%	0,62	0,667	0,75	0,82
100%	0,66	0,71	0,79	0,85

c) sideslip angle β [deg] TRACKER

c_{T_R} \ c_{T_L}	0%	20%	30%	40%
20%	13,46			
30%	15	7,18		
40%	14,78	9,65		
50%	15,38	9,98	5,9	
60%	16,06	11,85	4,13	1,94
70%	16,98	12,47	8,29	5,72
80%	16,07	13,28	9,06	7,15
90%	16,39	13,09	9,89	7,07
100%	16,53	13,72	9,7	9,61

d) sideslip angle β [deg] MATLAB

c_{T_R} \ c_{T_L}	0%	20%	30%	40%
20%	21			
30%	21,76	11,5		
40%	21,4	15		
50%	21,05	16,4	10	
60%	20,7	17,1	12	7,4
70%	20,4	17,5	13,3	9,5
80%	20,1	17,7	14,2	11
90%	19,9	17,8	14,8	12
100%	19,7	17,9	15,2	12,7

e) circulation radius [m] TRACKER

c_{T_R} \ c_{T_L}	0%	20%	30%	40%
20%	0,53			
30%	0,49	1,25		
40%	0,54	0,97		
50%	0,48	0,84	1,64	
60%	0,47	0,74	1,63	1,68
70%	0,47	0,74	1,49	1,33
80%	0,48	0,72	1,24	1,31
90%	0,48	0,61	1,08	1,37
100%	0,48	0,57	1,04	0,79

f) circulation radius [m] MATLAB

c_{T_R} \ c_{T_L}	0%	20%	30%	40%
20%	0,57			
30%	0,55	1,3		
40%	0,55	0,95		
50%	0,55	0,86	1,58	
60%	0,59	0,82	1,25	2,1
70%	0,6	0,8	1,1	1,6
80%	0,62	0,77	1,05	1,38
90%	0,65	0,75	0,97	1,25
100%	0,66	0,75	0,92	1,15

Fig. 17. Comparison of the experimental results with the simulation for circular motion (own elaboration)

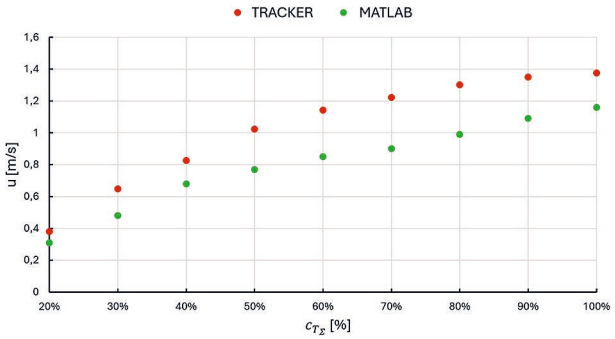

Fig. 18. Vehicle's forward velocity in steady state linear motion (own elaboration)

5. Discussion

Simplifications applied of the vehicle's mathematical model (reduced to 5DoF), the thrusters model, and the CFD analysis model required the tuning of the drag coefficients $C_{S\beta}$, $C_{m\beta}$ and M_{mr} obtained from the CFD through a simple scaling by a factor of 2. Additionally, the thrusters model was refined using manufacturers data and by accounting for thrust reduction when the vehicle is in motion, as reported in the literature. This approach produced similar circulation radii in both the experiment and the simulation (figures 17e and 17f). With these adjustments, the vehicle's forward velocity and sideslip angle in subsequent simulations showed good agreement with the experimental

results. A slight discrepancy can be observed in the velocity values at higher thrust percentages applied to both thrusters (reddish cells in figures 17a and 17b). The simulation model predicts lower velocities at high thrust, which may indicate an underestimation of thrust in the thruster model at higher control inputs. The highest sideslip angle β was obtained for the lowest circulation radii (figures 17c and 17d) and relatively low forward velocity, when only right thruster generated thrust. As the circulation radius and forward velocity increased, the dynamic stability of the vehicle's motion improved, as reflected by the decreasing sideslip angle. This trend was observed both in the experiment and in the simulation but β values are generally higher in the simulation, suggesting that the hydrodynamic stability effects of the hull may not be fully captured in the model. The circulation radii obtained experimentally are in good coincidence with the simulation results, although the model predicts slightly larger radii at higher thrust levels. This discrepancy again may result from the underestimation of thrust at higher settings.

The difference in forward velocity values during straight-line motion is due to the fact that the real vehicle operated at the water surface, while the Matlab® simulation assumed fully submerged vehicle, where additional drag was generated by the mast. As shown in Fig. 18, the mast generates significant drag, reducing the simulated vehicle's velocity. This issue will be addressed in future research, which will involve the development of a full underwater motion capture system for the vehicle.

Accurate knowledge of forward velocity, sideslip angle, and circulation radius is essential for controlling a group of vehicles, particularly during close-proximity maneuvers that are critical for collision avoidance. The proposed simulation model reproduces the experimental trends well and can therefore be used to test swarm control algorithms in future studies, though minor refinements to the thruster model may still be required.

6. Summary

This article presents a 5-DoF mathematical model of the HUVV based on the Fossen framework, with particular emphasis on the sideslip angle and variations in the propellers' thrust during motion. The model was implemented in MATLAB®. Its parameters, including various drag coefficients, were obtained from CFD analysis performed in SimScale® and subsequently tuned using data from the experiment. The added mass coefficients in the model were calculated analytically using methods found in the literature. Experimental verification of the proposed model was carried out through motion tracking of a real vehicle in a swimming pool. A GoPro Hero 6 camera suspended on a pendulum above the pool, along with Tracker® video analysis and motion tracking software, was used to measure the vehicle's forward velocities, sideslip angles, and circulation radii for various thrust settings of the left and right thrusters. The obtained results show good agreement with the simulation model, although minor adjustments to the thruster model are still required. Nevertheless, the developed simulation model is sufficiently accurate to support the future development of swarm control algorithms, which will later be validated using a group of four identical HUUVs and an underwater motion capture system.

https://doi.org/10.37705/TechTrans/e2025031

References

Bluerobotics. (2025). *T200* thruster data. Retrieved from https://bluerobotics.com/store/thrusters/t100-t200-thrusters/t200-thruster-r2-rp/ (date of access: 2025/11/4).

Chan, W. L., & Kang, T. (2011). Simultaneous determination of drag coefficient and added mass. *IEEE Journal of Oceanic Engineering*, *36*(3), 422–430. https://doi.org/10.1109/JOE.2011.2151370

Da Silva, J. E., et al. (2007). Modeling and simulation of the LAUV autonomous underwater vehicle. *13th IEEE IFAC International Conference on Methods and Models in Automation and Robotics*, Szczecin, Poland.

Foroushani, J. A., & Sabzpooshani, M. (2021). Determination of hydrodynamic derivatives of an ocean vehicle using CFD analyses of synthetic standard dynamic tests. *Applied Ocean Research*, *108*. https://doi.org/10.1016/j.apor.2021.102539

Fossen, T. I. (1994). *Guidance and control of ocean vehicles*. Wiley.

Fossen, T. I. (2011). *Handbook of marine craft hydrodynamics and motion control*. Wiley.

Gracey, W. (1941). *The additional-mass effect of plates as determined by experiments* (Report No. NACA-TR-707). National Advisory Committee for Aeronautics.

Jurczyk, K., Piskur, P., & Szymak, P. (2020). Parameters identification of the flexible fin kinematics model using vision and genetic algorithms. *Polish Maritime Research*, 27(2), 39–47. https://doi.org/10.2478/pomr-2020-0025

Kim, K., & Choi, H. S. (2007). Analysis on the controlled nonlinear motion of a test bed AUV-SNUUV I. *Ocean Engineering*, *34*(8–9), 1138–1150. https://doi.org/10.1016/j.oceaneng.2006.08.011

Lam, J., et al. (2023). Propeller characterization testing of a Blue Robotics T200 thruster. In *OCEANS*. IEEE. https://doi.org/10.1109/OCEANSLimerick52467.2023.10244513

Le, T. L., & Hong, D. T. (2021). Computational fluid dynamics study of the hydrodynamic characteristics of a torpedo-shaped underwater glider. *Fluids*, *6*(7). https://doi.org/10.3390/fluids6070252

Moelyadi, M. A., & Riswandi, B. B. (2018). CFD-based added mass prediction in cruise condition of underwater vehicle dynamic. Journal of Physics: Conference Series. https://doi.org/10.1088/1742-6596/1005/1/012011

Morawski, M., et al. (2018). Hardware and low-level control of biomimetic underwater vehicle designed to perform ISR tasks. *Journal of Marine Engineering and Technology*, *16*(4). https://doi.org/10.1080/20464177.2017.1387089

Newman, J.N. (1977a). *Marine hydrodynamics*. MIT Press. https://doi.org/10.7551/mitpress/4443.001.0001

Newman, J.N. (1977b). *Marine hydrodynamics*. MIT Press. https://doi.org/10.7551/mitpress/4443.001.0001

Szymak, P., et al. (2021). *Modeling and simulation of innovative autonomous underwater vehicle PAST*. In *2nd International Conference of Maritime Science & Technology*. University of Dubrovnik Maritime Department. Retrieved from https://www.researchgate.net/publication/357164323

Piskur, P., et al. (2021). Innovative energy-saving propulsion system for low-speed biomimetic underwater vehicles. *Energies*, *14*(24). https://doi.org/10.3390/en14248418

Piskur, P., et al. (2025). Why the Fossen model is so popular for marine vehicles' dynamic analysis? In *Proceedings – European Council for Modelling and Simulation (ECMS)* (pp. 545–550). https://doi.org/10.7148/2025-0545

Prestero, T. (2001). *Verification of a six-degree-of-freedom simulation model for the REMUS autonomous underwater vehicle* (Master's thesis). Massachusetts Institute of Technology. https://doi.org/10.1575/1912/3040

Przybylski, M. (2019). Mathematical model of biomimetic underwater vehicle. In *Proceedings – European Council for Modelling and Simulation (ECMS)* (pp. 343–347). https://doi.org/10.7148/2019-0343

Sakaki, A., & Sadeghian Kerdabadi, M. (2020a). Experimental and numerical determination of the hydrodynamic coefficients of an autonomous underwater vehicle. *Scientific Journals of the Maritime University of Szczecin*, *62*(134), 124–135. https://doi.org/10.17402/427

Sakaki, A., & Sadeghian Kerdabadi, M. (2020b). Experimental and numerical determination of the hydrodynamic coefficients of an autonomous underwater vehicle. *Scientific Journals of the Maritime University of Szczecin*, *62*(134), 124–135. https://doi.org/10.17402/427

Shrivastava, A., Karthikeyan, M., & Rajagopal, P. (2021). Modelling and motion control of an underactuated autonomous underwater vehicle. In *2021 6th Asia-Pacific Conference on Intelligent Robot Systems (ACIRS)* (pp. 62–68). https://doi.org/10.1109/ACIRS52449.2021.9519334

Society of Naval Architects and Marine Engineers. (1950). *Nomenclature for treating the motion of a submerged body through a fluid. Report of the American Towing Tank Conference*. New York.

Steenson, L. V., et al. (2012). Effect of measurement noise on the performance of a depth and pitch controller using the model predictive control method. *AUV 2012*. https://doi.org/10.1109/AUV.2012.6380732

Suzuki, H., et al. (2013). Evaluation of methods to estimate hydrodynamic force coefficients of underwater vehicles based on CFD. In *IFAC Proceedings Volumes* (pp. 197–202). https://doi.org/10.3182/20130918-4-JP-3022.00026

Tae Kyu Ha, et al. (2008). Sliding mode control for autonomous underwater vehicle under open control platform environment. In *SICE Annual Conference 2008*. The University of Electro-Communications, Japan.

Talarczyk, T. (2023a). A dynamic submerging motion model of the hybrid--propelled unmanned underwater vehicle: Simulation and experimental verification. *International Journal of Applied Mathematics and Computer Science*, *33*(2), 207–218. https://doi.org/10.34768/amcs-2023-0016

Talarczyk, T. (2023b). A dynamic submerging motion model of the hybrid--propelled unmanned underwater vehicle: Simulation and experimental verification. *International Journal of Applied Mathematics and Computer Science*, *33*(2), 207–218. https://doi.org/10.34768/amcs-2023-0016

Tran, N. H., et al. (2016). Steering and diving control of a small-sized AUV. In *Lecture Notes in Electrical Engineering* (Vol. 371, pp. 619–632). https://doi.org/10.1007/978-3-319-27247-4_52

Wang, Z., et al. (2025a). Identification modeling and trajectory tracking of robotic fish with synergistic fins-body. *IEEE Transactions on Robotics.* https://doi.org/10.1109/TRO.2025.3621044

Wang, Z., et al. (2025b). Identification modeling and trajectory tracking of robotic fish with synergistic fins-body. *IEEE Transactions on Robotics*. https://doi.org/10.1109/TRO.2025.3621044/MM1

Watson, K.P., Webster, J.S., & Crane, J.W. (1993). Prediction of submersible maneuvering performance at high incidence angles. In *Proceedings of OCEANS '93*, Victoria, Canada. https://doi.org/10.1109/OCEANS.1993.326108

Xie, F., & Du, R. (2019). Central pattern generator control for a biomimetic robot fish in maneuvering. In *2018 IEEE International Conference on Robotics and Biomimetics (ROBIO)* (pp. 268–273). https://doi.org/10.1109/ROBIO.2018.8665047